Automotive Science and Engineering, Vol. 14, No. 3, (2024), 4449-4463

Iran University of Science and Technology

Automotive Science and Engineering

Journal Homepage: ase.iust.ac.ir

ISSN: 2008-9899

A comprehensive study on air transverse flow effects on the collision behavior of a supercooled water droplet

S.R. Hosseini[1], M. Moghimi[2*], N.M. Nouri[3]

[1]Ph.D. Student, School of Mechanical Engineering, Iran University of Science and Technology, Tehran, Iran.

[2]Associate professor, School of Mechanical Engineering, Iran University of Science and Technology, Tehran, Iran.

[3]Professor, School of Mechanical Engineering, Iran University of Science and Technology, Tehran, Iran.

ARTICLE INFO

Article history:

Received : 2 Apr 2024

Accepted: 6 Jul 2024

Published: 13 Aug 2024

Keywords:

Air transverse flow

Superhydrophobic pillared surface

Supercooled droplet

Impacting-freezing simulation

Rebound and adhesion

A B S T R A C T

The impact of a supercooled droplet on a surface is a primary challenge of many industrial and aeronautical processes. However, in some cases, such as frost formation on vehicle windshields or wind turbine blades, the supercooled droplet collision does not occur in stagnant air. In this study, for the first time, the effects of the air transverse flow (ATF) on the thermal-fluid behavior of a supercooled droplet were investigated numerically. Also, different patterns of a superhydrophobic pillared surface were used in 24 three-dimensional simulations in ANSYS Fluent software. The volume of fluid method is chosen for the simulation of the multiphase flow. The ATF forces, the freezing effects, and the surface tension forces are included in the Navier-Stokes equations. The freezing model is improved by the supercooling temperature consideration method. The results show that the ATF velocity reduces the separation time exponentially and helps the droplet bounce from the surface before freezing inception. However, the excessive increase in ATF velocity has the opposite effect and may prevent the droplet from detaching the surface due to notable drag. The best value of the ATF velocity is obtained to be 8 m/s, which reduces the separation time exponentially from 16.3 ms to 12.5 ms for a cold surface with a simple pillar pattern. The separation time is entirely affected by the simulation conditions and varies from 11.85 ms to 29.2 ms. The maximum spreading factor, despite the separation time, is seriously influenced by the void fraction percentage of different pillared surfaces and varies from 1.53 to 1.69.

1. Introduction

Water, according to its degree of purity, has the ability to remain in a liquid state even below freezing temperature, a phenomenon known as supercooled water. In other words, if the temperature of a droplet decreases continuously, it may remain liquid even below the freezing temperature. This state of water, which is called a metastable state, is not permanent. It may freeze upon any water impurity or the slightest disturbance that enters the droplet boundary or due to contact with a surface boundary, regardless of boundary conditions. Although the pressure change does not affect the supercooling temperature limits considerably [1], it has some effect on the freezing process. The freezing process starts a little earlier at lower ambient pressure [2]. If the pressure of a room-temperature droplet

*Corresponding Author
Email Address: moghimi@iust.ac.ir
https://doi.org/10.22068/ase.2024.685

[DOI: 10.22068/ase.2024.685]

decreases continuously, its temperature lowers too and reaches the supercooling conditions [3].

The air temperature decreases linearly until -60 ℃, as we ascend from the earth surface (up to 10 km). So, the formation of supercooled droplets and their impact on different surfaces is a commonly observed occurrence in nature, aeronautical and various industrial processes, or any outdoor devices [4]. This collision can be inconvenient in many cases [5], such as poor visibility through the vehicle windshields [6], power transmission lines [7], airplane wings [8], pin insulators [9], wind turbine blades [10], , etc. It becomes essential to devise solutions to overcome probable challenges. Active anti-freezing techniques like mechanical vibration or thermal heating are expensive because consuming a lot of energy. Therefore, passive methods, which are mostly inspired by nature, should be more developed.

For example, applications of this phenomenon in vehicles are shown in Figure 1 and Figure 2.

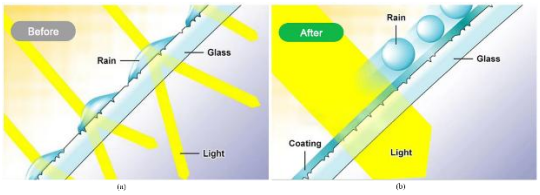

Figure 1: Effects of superhydrophobic coating on car windshield. (a) Spreading water droplets on the car glass causes the light to distort and as a result reduce the driver's vision. (b) The superhydrophobic coating cause droplets to blown away quickly by the wind.

Figure 1 depicts what happens to a driver's vision when raindrops collide with the surface of the windshield. The car glass looks smooth. But in fact, as seen in Figure 1, this surface is rough and therefore raindrops spread on the surface and obstruct the driver's vision. If superhydrophobic coatings are used on the glass surface, as seen in Figure 1-b and Figure 2, the probability of car accidents on rainy and snowy days is greatly reduced.

Recently, the dynamic behavior of impacting supercooled droplets on superhydrophobic and other various cold surfaces has been widely investigated [11]. Superhydrophobic surfaces were the first idea for anti-icing applications [12], [13]. These surfaces were inspired by lotus leaves or duck feathers. Some researchers have shown that superhydrophobic surfaces do not always work well in antifreeze applications and should be more advanced [14]. However, other researchers have been able to achieve good results with supercooled droplets by applying restrictions and limitations [15]. Wang et al. employed the dynamic contact angle to enhance the accuracy of simulations. They claimed if the Weber number ($We = \rho U^2 D/\sigma$) - the ratio of dynamic pressure (i.e., inertia force) to the surface tension force - was low (up to 40), the spreading factor of water droplets (i.e., the spreading diameter proportion to its primitive or $\beta = D/D_0$) in supercooled and room-temperature conditions were nearly equal. However, notable differences emerged at high Weber numbers (above 40). Furthermore, they illustrated that the Weber number did not affect the end-stage spreading factor. Even though it increased with both the contact angle reduction and the increment of the supercooling temperature [16].

Figure 2: (a) Frost formation is one of the main challenges of cold region drivers. Effect of superhydrophobic coating on (b) rear-view mirror and (c) front windshield. (d) Mechanical defrosting is only suitable for when the car is in park mode.

To improve the surface anti-icing features, a variety of micro and nano-structures with different morphologies and low-energy materials have been built. Surface asperities reduced the contact area between droplets and the surface, diminishing the likelihood of droplet freezing. For instance, Alizadeh et al. have highlighted the substantial impact of temperature on droplet collision with various surfaces. The significant temperature sensitivity observed on hydrophilic surfaces (contact angle, $\theta = 44°$) emphasizes the necessity for further analysis before considering these surfaces for applications like wicking or oil-water separation. Conversely, textured superhydrophobic surfaces (contact angle, $\theta = 149°$) exhibit consistent impact dynamics regardless of temperature variations (from -15 ℃ to 85 ℃), enhancing their appeal for applications in both low and high-temperature environments [17]. Shen et al. explored the icephobic properties of hierarchical superhydrophobic surfaces, which were developed through a combination of sandblasting and

[DOI: 10.22068/ase.2024.685]

hydrothermal treatment. As a result, this mechanism directly resulted in an extended delay in the icing time (750.4 s) and a low ice adhesion strength (80 kilopascals) at -10 ℃ [18]. Micro-nano structures consist of many minor pillars on a flat surface. They were instrumental in trapping a significant amount of air beneath the droplet, leading to diminished heat conduction efficiency between the water droplet and the cold solid surface [19].

Not only does the contact area influence droplet freezing, but the duration of contact also holds significant importance in the icing process when droplets impact a surface. This contact time dictated the exchange of momentum, mass, and energy between the droplet and the underlying surface [20]–[22]. Gauthier et al. explored how the inclusion of macro-textures (a wire with a radius of 100 μm) on superhydrophobic materials could significantly alter the dynamics of water droplets impacting these surfaces. Specifically, they noted a considerable reduction (from 13 ms to 7.6 ms) in the contact time of bouncing drops in the presence of macro-textures compared to a flat surface [23]. Vazirinasab et al. conducted a comparison between two superhydrophobic surfaces with distinct surface morphologies achieved through direct replication and plasma-treatment methods. Consequently, the first surface adopted a micro-structure, while the second exhibited a micro-nano-structure. The micro-structured surface notably delayed the initiation of freezing for a water droplet (3753 s), primarily attributed to the presence of larger micro-air pockets trapped within its surface asperities. On the other hand, the micro-nano-structured surface demonstrated a more significant reduction (about double) in ice adhesion compared to the micro-structured surface [24].

The impact of a supercooled droplet on a surface does not always occur in stagnant air. In many industrial activities, like frost formation on vehicle windshields or wind turbine blades, the process of collision and freezing for a droplet occurs along with air transverse flow (ATF). In addition, if different aspects of the ATF are discovered, artificial ATF can be made to achieve specific goals, such as influencing the freezing behavior of the impacted droplet. Since the presented investigation in this article is basically new, there is not exactly the same case as our study in the literature. Based on our research, the supercooled droplet hitting a pillared surface along with ATF was not studied numerically or experimentally. Most of the works were either without the presence of ATF [25], or if ATF was present, the droplet was descending in a free-falling manner and did not collide with the surface [26], [27], or the droplet was stationary on the surface [28], [29], or the coalescence of two sessile droplets was investigated [30]. In this study, for the first time, we investigate the supercooled droplet collision on surfaces that are exposed to different ATF velocities. Also, investigating the effects of the ATF on different pillar patterns as one of the main influencing parameters is considered. In this study, 24 three-dimensional simulations are performed in ANSYS Fluent software to find a comprehensive understanding of these issues.

2. Methodology

2.1. Governing equations

In the context of droplet collisions, it is essential to choose a multiphase flow model. For every phase (air and water droplet) in all equations, the Volume of Fluid (VoF) method [31] is commonly employed. For obtaining accurate results from simulations, the total simulation domain must be divided into very small grids or computational cells called grid generation. A continuity equation is employed to delineate the interface between different phases in each cell. As a result, the air volume fraction (α_1) and the water droplet volume fraction (α_2) are obtained for each cell, which are defined as:

$$\alpha_1 = \frac{air\ volume}{volume\ of\ cell} \quad \alpha_2 = \frac{water\ droplet\ volume}{volume\ of\ cell} \tag{1}$$

Also, in each computational cell, the following equation is established:

$$\alpha_1 + \alpha_2 = 1 \tag{2}$$

For example, if we have no water droplet in one cell, the volume of that cell will be definitely full of air. So, α_1 will be equal to 1, and α_2 will be equal to 0.

To express the mass conservation, we can utilize (3):

$$\frac{\partial}{\partial t}(\alpha_m \rho_m) + \boldsymbol{\nabla} \cdot (\alpha_m \rho_m \boldsymbol{u}) = 0\,; m = 1, 2 \tag{3}$$

where ρ means density, and $\boldsymbol{u}$ is the velocity vector. Nevertheless, for each cell of the domain, the momentum conservation is:

$$\frac{\partial}{\partial t}(\rho \boldsymbol{u}) + \boldsymbol{\nabla} \cdot (\rho \boldsymbol{u}\boldsymbol{u}) = -\boldsymbol{\nabla} \mathrm{p} + \boldsymbol{\nabla} \cdot \mu[\nabla \boldsymbol{u} + (\nabla \boldsymbol{u})^{\mathrm{T}}] + \rho \boldsymbol{g} + \boldsymbol{F}_{frz} + \boldsymbol{F}_{Tens} + \boldsymbol{F}_{ATF} \tag{4}$$

whereas p, μ, and $\boldsymbol{g}$ are the pressure, dynamic viscosity, and gravitational acceleration vector, respectively. Also, $\boldsymbol{F}_{frz}$ (will be introduced in (18)) represents the influences of the freezing process, $\boldsymbol{F}_{ATF}$ is the ATF force, which is actually

[DOI: 10.22068/ase.2024.685]

the drag force, and $\boldsymbol{F}_{Tens}$ signifies the surface tension effects, more precisely, the model of continuum surface force (CSF) [32]. Scientific reports show that the CSF closely matches empirical observations [33], which is calculated from the following equation:

$$\boldsymbol{F}_{Tens} = \sigma \frac{\rho \kappa \nabla \alpha_1}{\bar{\rho}} \quad (5)$$

Here, σ is the surface tension that equals 0.072 (N/m), κ represents the curvature of the droplet boundary, and $\bar{\rho}$ denotes the mean density of the air and the water droplet. The drag force calculation depends on the drag coefficient, C_D, which is approximately equal to 0.6 for a sphere [34] in the given range of ATF Reynolds number (below 3300) in this study. So, its magnitude is calculated as follows:

$$|\boldsymbol{F}_{ATF}| = |\boldsymbol{F}_{Drag}| = \frac{\rho V^2 C_D \pi D^2}{8} \quad (6)$$

where V and D denote the ATF velocity and droplet diameter. All fluid properties, for example (X), are calculated as:

$$\mathrm{X} = \sum_m \alpha_m \mathrm{X}_m \quad , \quad m = 1, 2 \quad (7)$$

All the values for fundamental physical properties employed in our simulation are given in Table 1.

Table 1. Material properties [35]

	$\rho\ (\frac{kg}{m^3})$	$c\ (\frac{J}{kg.K})$	$k\ (\frac{w}{m.k})$	$\mu\ (\frac{kg}{m.s})$	Latent heat $(\frac{kJ}{kg})$
Air	1.225	1006.43	0.0242	1.78 e -5	–
Water	998.2	4182	0.6	0.001003	333.4
Ice	916	2100	2.16	–	333.4

2.2. Taking into account the supercooling temperature

When a cold solid surface is impacted by a supercooled water droplet, it introduces additional stages compared to what is typically observed with isothermal normal conditions. In the normal condition (25℃), the impacted droplet spreads. After that, depending on the surface properties and droplet velocity, the droplet either sticks to the surface or rebounds [36]. On the other hand, in the supercooled condition, we have additional states such as nucleating, recalescence, and icing [37]. The impact process induces vibrations, triggering the freezing procedure [38]. The subsequent recalescence step initiates and concludes within a moment [39]–[41]. Consequently, neglecting the time associated with the first two stages, the impact moment must be taken into account as the primary condition at the commencement of the simulation. In simpler terms, prior to impact ($t = 0$), the supercooled droplet exists entirely in a liquid state, with zero-condition values of velocity (U_0), diameter (D_0), and supercooling temperature (T_0). However, at the instant of collision, supercooling droplets swiftly transform into a water-ice mixture ($T_{new} = T_S = 0$ ℃), consequently leading to changes in diameter or other properties of the droplet [42]. Therefore, from now on, we use the subscript "initial" to specify droplet properties at the start of the simulation.

2.2.1. Calculating the initial condition of simulations

If the energy conservation equation is written between zero time ($t = 0$) and new initial conditions, the initial ice fraction ($\delta_{initial}$) within the water-ice droplet is expressed as:

$$\delta_{initial} = \frac{c_{water,T_S}(T_S - T_0)}{L} \quad (8)$$

where L is the latent heat of freezing, and c is the specific heat, which both are given in Table 1. All physical attributes, for example (X), can be delineated as:

$$X_{initial} = (1 - \delta_{initial}) X_{water} + \delta_{initial} X_{ice} \quad (9)$$

The initial latent heat and the initial diameter are:

$$L_{initial} = (1 - \delta_{initial}) L \quad (10)$$

$$D_{initial} = \left(\frac{\rho_{water}}{\rho_{initial}}\right)^{1/3} D_0 \quad (11)$$

In general, the ice fraction can be computed using the following formula:

$$\delta = \begin{cases} 1 & T < T_{Solidus} \\ \frac{T_{Liquidus} - T}{T_{Liquidus} - T_{Solidus}} & T_{Solidus} < T < T_{Liquidus} \\ 0 & T > T_{Liquidus} \end{cases} \quad (12)$$

According to the states of droplets that are entirely water or entirely ice, their temperatures are known as the liquidus or solidus temperature. For the present study, $T_{Liquidus} = 0.1$ ℃ and $T_{Solidus} = -0.1$ ℃ [38]. Therefore, as in the above equations, it can also be said for the initial temperature:

$$T_{initial} = (1 - \delta_{initial}) T_{Liquidus} + \delta_{initial} T_{Solidus} \quad (13)$$

2.3. Freezing model

As we know, this study considers the initial water-ice mixture to be a liquid phase. Calculating the liquid fractions of all cells is achieved by employing the porosity-enthalpy method for modeling the solidification procedure. The summation of sensible heat and latent heat will be

[DOI: 10.22068/ase.2024.685]

equal to the overall enthalpy. The following equations are established.

$$h = h_{Sens} + h_{Lat} \quad (14)$$

$$h_{sens} = h_{T=0} + \int_0^T cdT \quad (15)$$

while $h_{T=0}$ represents the enthalpy of water at 0 ℃, which equals 0.06 (kJ/kg). The latent heat is given by:

$$h_{Lat} = (1-\delta)L_{initial} \quad (16)$$

Therefore, the conservation of energy is following:

$$\frac{\partial}{\partial t}(\rho h) + \boldsymbol{\nabla}\cdot(\rho \boldsymbol{u} h) = \boldsymbol{\nabla}\cdot(k\boldsymbol{\nabla}T) \quad (17)$$

Absolutely, the enthalpy-porosity model incorporates the concept of a mushy zone, which mimics a porous medium within the system. In simulations involving very pure water, the existence of a mushy zone may not be evident. However, in most simulations, it is a critical consideration. During a water droplet freezing, the liquid fraction of a cell aligns with its porosity, diminishing from 1 to 0. The porosity of the droplet in a cell becomes zero when it is completely frozen, leading to a zero velocity. In order to guarantee zero velocity, it is necessary for the momentum equation to include the freezing term ($\boldsymbol{F}_{frz}$) and its appropriate form. Here is how to do it:

$$\boldsymbol{F}_{frz} = \frac{\delta^2}{(1-\delta)^3+\varepsilon} A_{mush}\boldsymbol{u} \quad (18)$$

Adding a small number ($\varepsilon = 0.001$) to the denominator is a practical step to prevent division by zero. The mushy zone constant, A_{mush}, plays a crucial role in determining how rapidly the velocity approaches zero during solidification. As A_{mush} increases, the velocity will move more quickly to zero. A range of values, typically suggested [43], spans from 10^4 to 10^7. Optimal selection is essential as manifestations of velocities in the frozen area may be shown by smaller values, while greater A_{mush} might introduce numerical oscillations. The freezing time is directly correlated to the mushy zone, as well as the supercooling temperature, T_0, suggesting a potential correlation between these variables. This empirical relationship is detailed in Table 2.

Table 2. Empirical correlation of supercooling temperature and A_{mush} [44].

Supercooling temperature T_0(℃)	-5	-10	-15	-20
A_{mush}	10^4	5×10^4	10^5	5×10^5

2.4. Validation of the numerical model

Comparing numerical results with experimental data is a necessary approach to validate the accuracy and reliability of simulations. In this case, two experiments by Zhang et al. [44] were considered for comparison. The first experiment explored the room-temperature collision of a droplet with an isothermal surface. The second experiment investigated the collision of a supercooled droplet with a cold surface and the freezing process. The hitting velocity, Weber number, and initial droplet diameter of both experiments were consistent with 0.7 m/s, 19.18, and 2.84 mm, respectively. The dynamic contact angle measurements of the surface were 160°$\pm$ 2°. All the temperatures in isothermal conditions were 15 ℃. On the other hand, in the supercooled condition, the temperature of the surface was -30 ℃, while the temperature of the droplet and its surroundings was -5 ℃. The physical properties are given in Table 1. The contact angle of the droplet would change continuously during the impacting process. So, instead of a static contact angle, a dynamic contact angle should be used to capture the contact line speed accurately [45]. In accordance with the Kistler model [46], which delivers outcomes that have a reliable match with experimented records [47], a user-defined function (UDF code) was prepared and embedded into ANSYS Fluent to calculate the dynamic contact angle in each time step. According to our computing equipment (a computer with a 4.0 GHz CPU and a 32.0 GB RAM), each simulation took ten days to complete.

In the first case (i.e., Figure 3-a), the droplet exhibits a detachment, whereas an adhesion droplet occurs in another because of supercooling condition (i.e., Figure 3-b). Solidification is initiated promptly as soon as a supercooled droplet collision occurs, leading to stabilization of the wetted area of the droplet. Meanwhile, the rest of the droplet volume is not frozen and attempts to rebound, resulting in droplet stretching. In certain cases, the tip of the droplet might even detach and move upward. Essentially, there is a simultaneous observation of the progression of heat transfer (at the droplet bottom) and droplet dynamics (at the droplet tip).

[DOI: 10.22068/ase.2024.685]

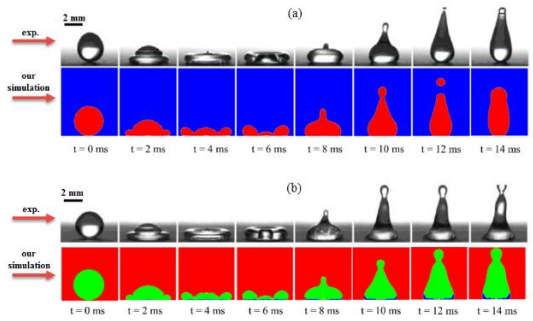

Figure 3: Qualitative comparison of (a) an isothermal and (b) a supercooled droplet impact between the experimental observations by [44] and the present numerical results.

A more accurate and quantitative comparison for validation is given in Figure 4. As depicted, there exists a slight difference between our numerical simulations and the experimental data. The maximum standard deviation in the isothermal case is 18%, and in the supercooled condition is 11%. However, this deviation is deemed acceptable given the complexities involved in simulating the droplet dynamics and phase change of a supercooled droplet.

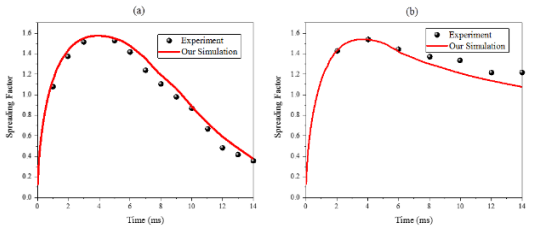

Figure 4: Quantitative comparison of (a) an isothermal and (b) a supercooled droplet impact between the experimental observations by [44] and the present numerical results.

3. Numerical simulation procedure

Using ANSYS Fluent software, the three-dimensional simulation of a supercooled (-5 ℃) droplet impact on a cold (-30 ℃) surface was established. The droplet diameter was 3 mm, its velocity at the collision moment was 0.7 m/s, and the Weber number was 20.417. The maximum Courant number (a dimensionless value representing the number of mesh cells traveled at a given time step, $C = u\Delta t/\Delta x$ where C is Courant number, u is velocity magnitude, Δt is time step size, and Δx is the length between mesh elements) was set to 0.2. The surface was composed of cubic pillars with 0.2 mm edges. The space between the pillars was also 0.2 mm. The ATF entered the domain with a certain velocity as opposed to the X direction. To model the freezing process, the solidification model of software was adjusted with the supercooled condition requirements, which were explained in Sec. 2.2. The liquidus and solidus temperatures were 0.1 ℃ and -0.1 ℃, respectively, and the mushy zone constant (A_{mush}) was 10^5 in all simulations. The initial temperature of the air and the temperature of the domain boundaries are equal to the liquidus temperature. The boundary conditions and the domain size - in terms of droplet diameter (D_0) - were shown in Figure 5. The boundary conditions for the left side (ATF in) and the right side (ATF out) were *velocity inlet* and *pressure outlet*, respectively. The boundary conditions of the three lateral sides were *symmetry*. As shown in Figure 5, the symmetry plane, which was unique with ABCD letters, split the droplet and domain into two equal parts. Therefore, only half of the droplet and domain were simulated. A structured and fined mesh was used in all simulations to improve the accuracy and to obtain precise liquid-gas interface calculations. Around the droplet and its impact place, the cubic grid size was refined to 40 μm for each edge of a cell.

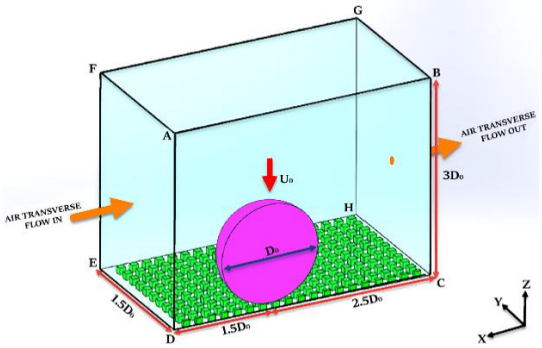

Figure 5: Schematic model of the domain simulations.

3.1. Investigated cases

In this work, to study the effects of ATF velocity on a cold pillared surface that is impacted by a supercooled droplet, 24 simulations have been performed in different conditions and with varying input values. The specifications of these 3D simulations are shown in Table 3. One of the main parameters was the velocity of ATF. The simulations were performed with different ATF velocities from 0 to 16 m/s. Considering the diameter of the droplet, which was 3 mm, the Reynolds number of ATF is less than 3300 in all simulations. Another parameter that has been investigated is the arrangement of the pillars on the surface. In this study, five patterns specified in Figure 6 have been examined. Parameters such as

[DOI: 10.22068/ase.2024.685]

the Weber number and the height of the pillars have also been investigated briefly, which will be described later.

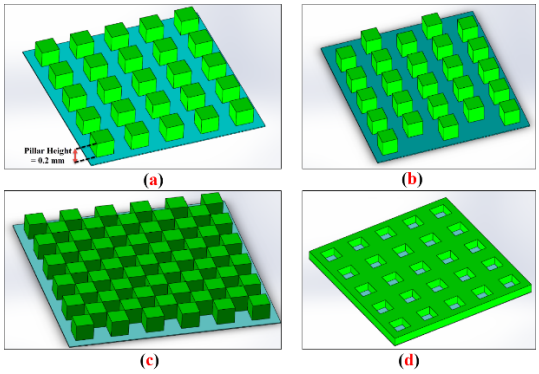

Figure 6: Five different examined patterns in this study: (a) a simple pattern, (b) a staggered pattern, (c) a checkered pattern, and (d) a hollow pattern. The fifth pattern was a flat (no-pillar) pattern, which is not shown. All dimensions (either all edges of cubic pillars and cubic hollows or all spaces between them) are 0.2 mm. The number of pillars and the domain size are schematic and not to scale.

Table 3. Specifications of all the simulations performed in this study.

Case number	ATF velocity (m/s)	Pillar pattern	Weber number	Pillar height (mm)
1	0	Simple	20.417	0.2
2	4	Simple	20.417	0.2
3	6	Simple	20.417	0.2
4	8	Simple	20.417	0.2
5	10	Simple	20.417	0.2
6	12	Simple	20.417	0.2
7	14	Simple	20.417	0.2
8	16	Simple	20.417	0.2
9	0	No-Pillar	20.417	0.2
10	0	Checkered	20.417	0.2
11	0	Staggered	20.417	0.2
12	0	Hollow	20.417	0.2
13	6	No-Pillar	20.417	0.2
14	6	Checkered	20.417	0.2
15	6	Staggered	20.417	0.2
16	6	Hollow	20.417	0.2
17	8	No-Pillar	20.417	0.2
18	8	Checkered	20.417	0.2
19	8	Staggered	20.417	0.2
20	8	Hollow	20.417	0.2
21	8	Staggered	60	0.2
22	8	Staggered	100.104	0.2
23	8	Simple	20.417	0.6
24	8	Staggered	20.417	0.6

3.2. Grid independence study

In order to check the grid independence of the numerical simulation results, four different grids were created, which divided the edge of each pillar into three, four, five, and six cells, respectively. As shown in Figure 6, the edge of each cubic pillar is 0.2 mm. Therefore, the fineness of the grids in each of the four modes is obtained. In these simulations, the ATF velocity is considered to be 4 m/s. The pillar patterns are simple. Other conditions are the same as the descriptions of Sec. 2.6. The physical properties are given in Table 1. For these four modes of grids, the spreading factors of droplets in terms of time are shown in Figure 7. All four diagrams are the same until the maximum spreading factor point. When the droplet starts to move back from the maximum point, the five-cell and six-cell diagrams are closer to each other, and the three-cell and four-cell diagrams are more different from these two. Due to computational limits, the five-cell grid is chosen as the best grid for all simulations of this work.

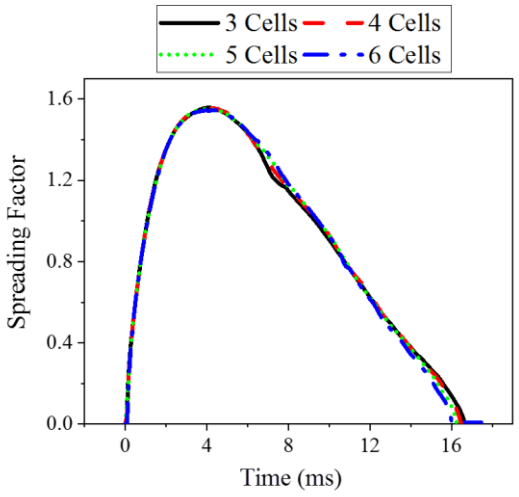

Figure 7: Examining mesh dependability based on how many cells there are inside one groove.

4. Results and Discussion

In order to investigate the effects of ATF on the impact of supercooled droplets in different situations, first, we set a simulation as the base simulation and analyze its results. Then, all the simulations were compared with the base one. The base simulation (i.e., the third case in Table 3) consists of the case where the pillared surface was simple, the Weber number was 20.417, the ATF velocity was 6 m/s, and the height of the cubic pillars was 0.2 mm. The volume fraction contour (at the symmetry plane) of this simulation was shown in Figure 8 at different times. The dashed line shown in Figure 8 demonstrated the initial point of droplet impact at the beginning. As seen in Figure 8, after the droplet impacted the surface, at early times (Figure 8-b, c, and d), there was a slight

[DOI: 10.22068/ase.2024.685]

deformation due to the ATF passing from the left to the right side. Then, the droplet was noticeably moved to the right (Figure 8-e) and was not symmetrical anymore. Also, the ATF influenced and raised the droplet's left part. Finally, two parts were created from the droplet (Figure 8-f), and then they were integrated again (Figure 8-g). Afterward, separation from the plane was started by the droplet (Figure 8-h, i, j), as it deformed thoroughly. The ATF stretched the droplet to the right and disturbed its original shape. Next, the droplet continued its attempt to separate from the surface (Figure 8-k) but could not entirely separate from the surface.

The reason was that the ATF contributed to the droplet's left part separation and the droplet's right part prevention from bouncing simultaneously. Therefore, the right side of the droplet met the surface again. Another reason was that due to the separation mode of the droplet, the droplet shape stretched, and the cross-sectional area of the droplet maximized. Therefore, the effect of ATF on the droplet increased. Finally, after separation of the left side and adhesion of the right successively, the droplet entirely separated from the surface (Figure 8-l). The bottom center of the droplet has been shifted by 1.2 mm in the horizontal direction from the beginning to separation.

After analyzing the base simulation, it is necessary to change the main parameters of the simulation in order to find out the effectiveness of each of them. In Table 3, the main specifications of all simulations are given. As mentioned before, five different pillar patterns were provided to thoroughly investigate the simulations by using different input parameters that were given in Table 3. The first comparison shown in Figure 9 was performed between the first four simulations from Table 3. The values of the spreading factor in terms of time were given for these four simulations. The Weber numbers were 20.417, and the cubic pillar height was 0.2 mm. A simple pattern was used for these four simulations. The only difference between these simulations was the ATF velocity. As shown in Figure 9, the maximum of the spreading factor values occurred in the first simulation of Table 3, which did not have ATF at all. In this simulation, the separation time (i.e., the time when the spreading factor became zero again) of the droplet was later than the three other simulations.

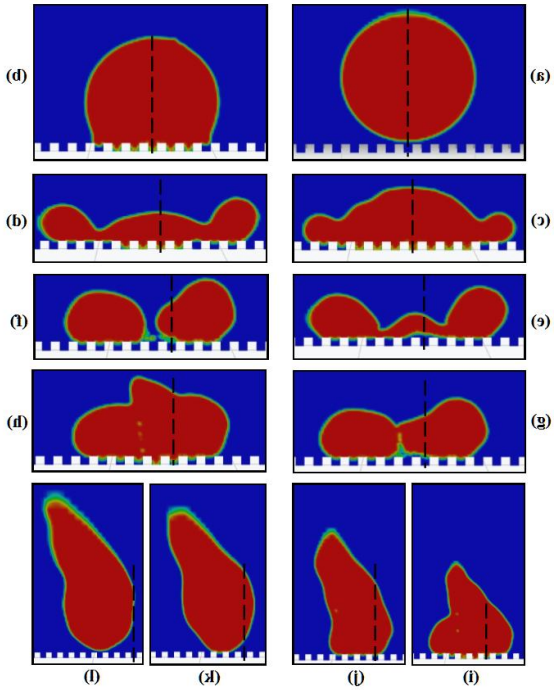

Figure 8: Contour of volume fraction at symmetry plane of the base simulation, the third case, at different times. (a): t = 0 ms, (b): t = 0.9 ms, (c): t = 3 ms, (d): t = 5 ms, (e): t = 6.5 ms, (f): t = 7.7 ms, (g): t = 7.8 ms, (h): t = 8.3 ms, (i): t = 9.5 ms, (j): t = 11 ms, (k): t = 12.9 ms, (l): t = 15.6 ms. The red and blue colors represent the water droplet and the air, respectively. The dashed line demonstrates the initial point of droplet impact at the beginning.

In the second simulation ($4\ m/s$), both the separation time and the maximum spreading factor decreased slightly. It showed that the ATF velocity of $4\ m/s$ did not have a considerable effect on these two parameters. In the third and fourth simulations ($6\ and\ 8\ m/s$), the maximum spreading factor did not change significantly, but as seen in Figure 9, the separation time decreased multiplicity.

The noteworthy point was that if we continued this process of increasing the ATF velocity, the droplet separation from the surface would not necessarily improve. Figure 10 shows the comparison of the next four simulations in Table 3. In these simulations, the ATF velocities were from 10 to 16 m/s. As seen in Figure 10, the maximum spreading factors decreased significantly because the ATF gained more dynamic energy and prevented the spreading processes after the droplet collisions. More importantly, their curves deviated from their usual process and found an oscillating state. Finally, the separation of droplets from surfaces not only did not occur earlier, but also droplets were entirely attached to surfaces.

[DOI: 10.22068/ase.2024.685]

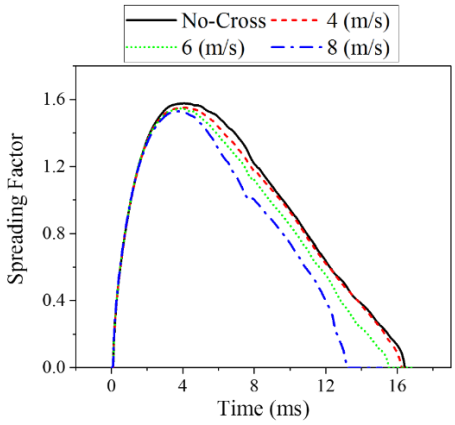

Figure 9: Comparison of spreading factors with different ATF velocities.

Except in the fifth simulation ($10\ m/s$), in three other simulations, the droplet could not be separated from the surface at all. It shows that the ATF velocity parameter does not always go through a uniform process, and it cannot be said that the more the ATF velocity, the faster the droplet will separate from the surface. The presence of multiple maximum and minimum points in this diagram indicates that the droplet's shape continuously changes and has a completely fluctuating behavior. It means that on the one hand, the kinetic energy of the droplet is trying to behave normally in impact and rebound. On the other hand, the high-speed ATF causes the droplet's shape to change and wastes the kinetic energy of the droplet. Therefore, the contact area of the droplet with the surface has decreased and increased several times.

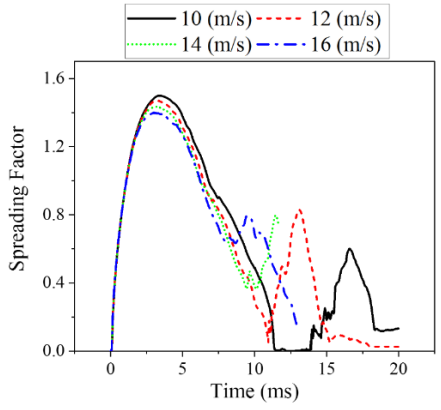

Figure 10: Excessively increasing the ATF velocity leads to fluctuations in the spreading factor, and the droplet separation may not occur at all.

To clarify, when there is an ATF and the surface is impacted by a droplet, depending on whether the ATF velocity is low, medium, or high, three situations occur. At low velocities (0 to $4\ m/s$), the droplet-surface adhesion becomes weak due to the shear stress applied to the droplet contact line. As a result, the droplet adhesion is reduced and can be separated easily and quickly from the surface. However, the amount of separation time and spreading factor reductions are insignificant owing to the low velocity.

At medium velocities (4 to $8\ m/s$), another factor affects the problem, and that is the droplet deformation. The horizontal force applied to the droplet changes its shape and prevents it from spreading. In this case, the droplet has an auxiliary force during the receding stage and for separation from the surface. That is, not only is the bond between the droplet and the surface weakened, but the entire cross-sectional area of the droplet from the left side is also affected by the ATF. The further the droplet goes in the receding and separation stage, the more the effect of this force increases due to the increase in the cross-sectional area. This force reaches its maximum value when the droplet is entirely stretched at the moment of its separation. For this reason, as seen in Figure 9, once the greatest spreading factor is approached and the stage of receding begins, the curves diverge from each other. As time passes, their distance from each other increases. Therefore, the detachment time decreases exponentially. At high velocities ($10\ m/s$ and above), the effects of ATF velocity become too large. Although the spreading factor has decreased significantly, the droplet cannot be separated from the surface at all because most of the droplet's kinetic energy is used to counter the drag force. As a result, the droplet does not have the opportunity to develop its kinetic energy at all, and as it is attached to the surface, it rolls on the surface and simultaneously slides and leaves the simulation domain. Therefore, it can be said that the increase in the ATF velocity had an optimal point, and in this study, the optimal velocity was 8 m/s.

Another parameter that could be investigated was the effect of changing the pattern of the surface pillars on the output parameters. As shown in Figure 6, five different patterns have been examined. The amount of void fraction (i.e., the empty space percentage) was different in these five patterns. The void fraction percentage for the simple and the staggered modes was 75%, for the checkered mode 50%, for the hollow mode 25%, and zero for the mode where there was no pillar at all. First, we examine the effects of pillar pattern on the droplet separation time among 15 simulations performed with different ATF velocities. As shown in Figure 11-a, the surface morphology, regardless of its void fraction percentage, had a significant effect on reducing the

[DOI: 10.22068/ase.2024.685]

droplet separation time and its non-freezing property. In the case where there is no ATF, the use of the pillar has almost halved the droplet separation time.

Another noteworthy point was that the droplet separation time did not have a linear relationship with the void fraction percentage. For example, in the case where there was no ATF and the void fraction was 75%, the droplet separation time was approximately 16.5 ms. Now, if we reduced the void fraction percentage to 25% (i.e., the hollow pattern), the separation time would increase, but only by 1.1 ms. However, if the void fraction became zero, the droplet separation time would be very long, i.e., 29.2 ms. It showed that the main and effective parameter in reducing the drop separation time was the discontinuity of the surface rather than the percentage of void fraction. Multiple and non-continuous connections and adhesions could not prevent the droplet from separating the surface, even if the density and number of these adhesions were high. As seen in Figure 11-a, the best performance in droplet separation was related to the case that the ATF velocity was 8 m/s, and the type of pillar pattern was staggered. Generally, the worst performance was related to the case where there was no ATF and no pillar.

The next point that could be seen in Figure 11-a was the close distance between the upper curve and the middle curve, in proportion to the distance between the middle and lower curves. It showed that the effectiveness of increasing the ATF velocity from 6 to 8 m/s was generally greater than from zero to 6 m/s. However, in the case without pillars, this was the opposite. For a more detailed comparison, the percentage of drop separation time reduction was shown in Figure 11-b in two different modes. The first mode was the change of the ATF velocity from zero to 6 m/s, and the second mode was the change of the ATF velocity from 6 to 8 m/s. As seen in Figure 11-b, in the case where the pillar pattern was hollow, increasing the ATF velocity from 0 to 6 m/s had no effect on reducing the droplet separation time, and in both velocities, the droplet left the surface in 17.6 ms. But, by increasing the ATF velocity from 6 to 8 $\mathrm{m/s}$, a significant decrease was suddenly observed at the time of droplet separation.

The next comparison is the examination of the greatest spreading factor through 15 simulations. As seen in Figure 12, the maximum spreading factor of the droplet shows a different behavior in relation to the droplet separation time.

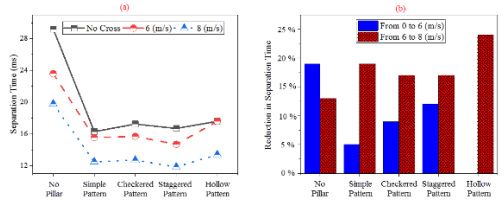

Figure 11: Comparison of (a) the rebounding time in different pillar patterns along with different ATF velocities and (b) the ATF velocity increment effects on the separation time.

As described before, the droplet separation in relation to the void fraction did not have linear behavior, and surface morphology was the main parameter influencing the drop separation (Figure 11-a). However, it can be seen here that the droplet maximum spreading factor was entirely proportional to the void fraction, and the changes followed a regular rule. The lowest amount of the maximum spread factor was related to the void fraction percentage of 75% (such as the staggered and the simple pattern). The checkered pattern with the void fraction percentage of 50% was in the next rank and had a greater amount of the maximum spreading factor. This regular trend continued in the hollow pattern with the 25% void fraction percentage and the no-pillar surface with zero void fraction. Also, as we increase the ATF velocity, the trend of decreasing the maximum spreading factor in Figure 12 is regular (unlike Figure 11-b) and is not exponential.

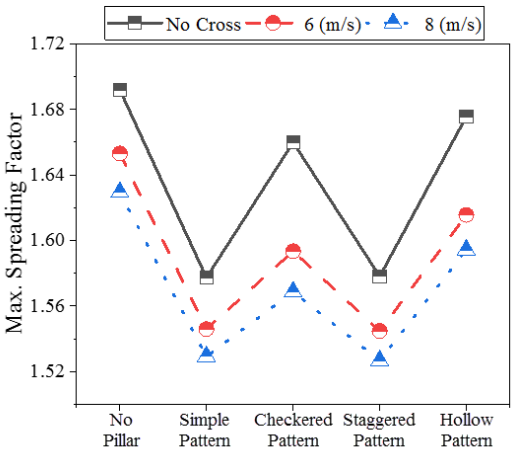

Figure 12: Comparison of the maximum spreading factor in different pillar patterns and different ATF velocities.

The droplet separation time and the droplet spreading factor were investigated in the following stage by examining the impact of increasing the Weber number. For this purpose, the 19th, 21st, and 22nd cases from Table 3 have been compared. As

[DOI: 10.22068/ase.2024.685]

seen in Table 3, the height of the pillars, the ATF velocity, and the type of patterns used in all three simulations were the same, and the only difference between these three simulations was their Weber numbers. The comparison of these three simulations is indicated in Figure 13. As seen, increasing the Weber number increases the maximum spreading factor of the droplet because the droplet impacts the surface with a higher speed and consequently spreads more.

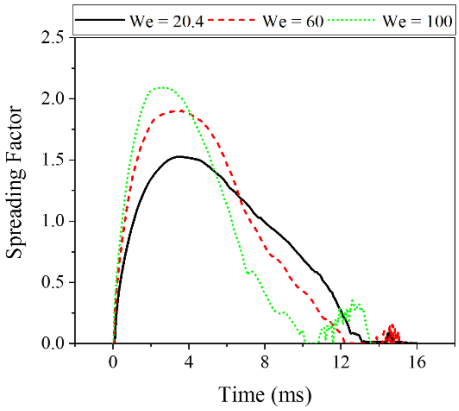

Figure 13: Effects of Weber number increasing on the spreading factor and the separation time.

On the other hand, due to the increased kinetic energy of the droplet, it had more energy to separate from the surface, and therefore, it separated faster. Also, the peak of the graph got closer to the vertical axis with the Weber number increasing. The next point is that the higher the Weber number was, the more likely the droplet would break into pieces after impact, especially if it was exposed to the ATF. As seen in Figure 13, with the increase of the Weber number, the fluctuation of the spreading factor, which was due to the fragmentation of the droplet, also increased. Therefore, there was a limitation in this aspect as well, and it was not possible to easily reduce the separation time by increasing the Weber number. In the last two simulations from Table 3, the effects of increasing the pillar height have been investigated. The results of these simulations showed that increasing the cubic pillar height from 0.2 mm to 0.6 mm decreased the maximum spread factor from 1.529 to 1.407. Changing the pattern from simple to staggered did not have much effect on this conclusion. Also, due to the increase in the height of the pillars, the droplet separation time has decreased from 11.85 ms to 11.75 ms in the staggered pattern and from 12.5 ms to 12.3 ms in the simple pattern. In summary, by having various analyses of how droplets behave in the presence of ATF, solutions can be found that increase the efficiency of wind turbine blades or increase the visibility of car drivers in cold regions.

5. Conclusions

This study examined how ATF affects the collision of supercooled droplets on cold pillared surfaces with five different morphologies. Eight Different ATF velocities with five different pillar patterns were compared numerically with each other. The main findings of these 24 three-dimensional simulations were:

1- Increasing the ATF velocity up to 8 m/s helped the impacting droplet to separate from the surface. For a cold surface with the simple pillar pattern, the separation time decreased exponentially from 16.3 ms to 12.5 ms. The spreading factor also decreased, but it was not significant.

2- Excessively increasing the ATF velocity above 10 m/s had the opposite effect on reducing droplet separation time. It led to fluctuations in the spreading factor, and the droplet separation might not occur at all.

3- The surface morphology, regardless of its pillar pattern and void fraction percentage, had a main effect (100% in some cases) on reducing the droplet separation time and its anti-freezing feature. The multiple and non-continuous adhesions could not prevent the droplet from separating the surface.

4- Contrary to the separation time, the behavior of the spreading factor was not exponential due to the change in the pattern of pillars and void fraction. Its behavior is entirely regular, and as the percentage of surface void fraction decreased, the value of the maximum spreading factor increased in the same proportion.

In this article, a comprehensive study about ATF was done for the first time. However, due to the lack of numerical or experimental data about this issue in literature, more numerical simulations or some experiments can be carried out to achieve higher reliability of the numerical model and enrich the numerical and experimental data. For example, one can experimentally investigate the impact of a supercooled droplet with a superhydrophobic surface in the presence of different ATF velocities. The temperature of ATF and its effect on rebounding is another subject that can be done in future both numerically and experimentally. Also, one can investigate periodic ATF cases or the coalescence of multiple droplets impacting a superhydrophobic surface in the presence of ATF [48], [49].

[DOI: 10.22068/ase.2024.685]

Declaration of Conflicting Interests

The author(s) declared no potential conflicts of interest with respect to the research, authorship, and/or publication of this article.

List of symbols

Letters

h	Enthalpy (J kg^{-1})
A_{mush}	Mushy zone constant
k	Thermal conduction coefficient (W m^{-1} K^{-1})
We	Weber number
$\boldsymbol{U}$	Velocity vector (m s^{-1})
V	Magnitude of ATF velocity
P	Pressure (N m^{-2})
$\boldsymbol{r}$	Unit normal vector (m)
T	Temperature (K)
L	Latent heat of solidification (kJ kg^{-1})
c	Specific heat (J kg^{-1} K^{-1})
D	Diameter (mm)
C_D	Drag coefficient

Greek symbols

α	Volume fraction
ρ	Density (kg m^{-3})
μ	Dynamic viscosity (kg m^{-1} s^{-1})
κ	Curvature (m^{-1})
σ	Surface tension (N m^{-1})
δ	Ice fraction
β	Spreading factor
θ	Contact angle (degree)

Subscripts

0	Before droplet impact (zero time)
initial	Immediately after droplet impact
S	Solidification point
m	The mth phase
Tens	Surface tension
Frz	Freezing process
Sens	Sensible
Lat	Latent

Acronyms

ATF	Air transverse flow
VoF	Volume of fluid

References

[1] A. Nilsson, "Origin of the anomalous properties in supercooled water based on experimental probing inside 'no-man's land,'" *J. Non-Crystalline Solids X*, vol. 14, p. 100095, Jun. 2022, doi: 10.1016/J.NOCX.2022.100095.

[2] Z. Jin, Y. Zhao, D. Sui, and Z. Yang, "The Effects of Ambient Pressure on the Initiation of the Freezing Process for a Water Droplet on a Cold Surface," *J. Heat Transfer*, vol. 138, no. 8, Aug. 2016, doi: 10.1115/1.4033377/454577.

[3] X. Yan *et al.*, "Unraveling the role of vaporization momentum in self-jumping dynamics of freezing supercooled droplets at reduced pressures," *Nat. Commun. 2024 151*, vol. 15, no. 1, pp. 1–10, Feb. 2024, doi: 10.1038/s41467-024-45928-2.

[4] X. Cheng, Y. Zhu, L. Zhang, C. Wang, and S. Li, "Lattice Boltzmann simulation of multiple droplets impingement and coalescence in an inkjet-printed line patterning process," *Int. J. Comut. Fluid Dyn.*, vol. 31, no. 10, pp. 450–462, Nov. 2017, doi: 10.1080/10618562.2017.1400021.

[5] J. Lv, Y. Song, L. Jiang, and J. Wang, "Bio-inspired strategies for anti-icing," *ACS Nano*, vol. 8, no. 4, pp. 3152–3169, Apr. 2014, doi: 10.1021/NN406522N/ASSET/IMAGES/MEDIUM/NN-2013-06522N_0008.GIF.

[6] K. Koshio, T. Waku, and Y. Hagiwara, "Ice-phobic glass-substrate surfaces coated with polypeptides inspired by antifreeze protein," *Int. J. Refrig.*, vol. 114, pp. 201–209, Jun. 2020, doi: 10.1016/J.IJREFRIG.2020.01.025.

[7] R. Liao *et al.*, "Ice accretion on

[DOI: 10.22068/ase.2024.685]

superhydrophobic insulators under freezing condition," *Cold Reg. Sci. Technol.*, vol. 112, pp. 87–94, Apr. 2015, doi: 10.1016/J.COLDREGIONS.2015.01.006.

[8] F. Mosher, D. Schaum, C. Herbster, and T. Guinn, "Analysis of causes of icing conditions which contributed to the crash of continental flight 3407," in *14th Conference on Aviation, Range, and Aerospace Meteorology*, 2010. Accessed: Jan. 03, 2023. [Online]. Available: https://commons.erau.edu/db-applied-aviation/21/

[9] X. Han and X. Jiang, "Effect of DC electric field on water droplets' movement and icing process on insulator," *Cold Reg. Sci. Technol.*, vol. 164, p. 102780, Aug. 2019, doi: 10.1016/J.COLDREGIONS.2019.102780.

[10] A. Aihara, M. Tanaka, and N. Fujisawa, "Influence of surface curvature on the impact force of water droplet," *J. Appl. Phys.*, vol. 136, no. 11, Sep. 2024, doi: 10.1063/5.0219757/3313339.

[11] X. Cui, W. G. Habashi, and V. Casseau, "Multiphase SPH Modelling of Supercooled Large Droplets Freezing on Aircraft Surfaces," *Int. J. Comut. Fluid Dyn.*, vol. 35, no. 1–2, pp. 79–92, Feb. 2021, doi: 10.1080/10618562.2020.1817401.

[12] Z. Zhu, X. Zhang, Y. Zhao, X. Huang, and C. Yang, "Freezing characteristics of deposited water droplets on hydrophilic and hydrophobic cold surfaces," *Int. J. Therm. Sci.*, vol. 171, p. 107241, Jan. 2022, doi: 10.1016/J.IJTHERMALSCI.2021.107241.

[13] W. Li, J. Wang, C. Zhu, L. Tian, and N. Zhao, "Numerical investigation of droplet impact on a solid superhydrophobic surface," *Phys. Fluids*, vol. 33, no. 6, 2021, doi: 10.1063/5.0050378.

[14] M. Dorrestijn, S. Jung, C. M. Megaridis, D. Raps, A. Das, and D. Poulikakos, "Are Superhydrophobic Surfaces Best for Icephobicity?," *Langmuir*, vol. 27, no. 6, pp. 3059–3066, 2011, doi: 10.1021/la104762g.

[15] H. Zhang, Y. Zhao, R. Lv, and C. Yang, "Freezing of sessile water droplet for various contact angles," *Int. J. Therm. Sci.*, vol. 101, pp. 59–67, 2016, doi: 10.1016/j.ijthermalsci.2015.10.027.

[16] Y. Wang, Q. Wang, L. Ju, D. Han, and Y. Xue, "Numerical analysis on dynamics and thermodynamics of a supercooled water droplet considering the dynamic contact angle," *Phys. Fluids*, vol. 33, no. 10, 2021, doi: 10.1063/5.0061621.

[17] A. Alizadeh *et al.*, "Temperature dependent droplet impact dynamics on flat and textured surfaces," *Appl. Phys. Lett.*, vol. 100, no. 11, pp. 2010–2014, 2012, doi: 10.1063/1.3692598.

[18] Y. Shen, H. Tao, S. Chen, L. Zhu, T. Wang, and J. Tao, "Icephobic/anti-icing potential of superhydrophobic Ti6Al4V surfaces with hierarchical textures," *RSC Adv.*, vol. 5, no. 3, pp. 1666–1672, 2015, doi: 10.1039/c4ra12150c.

[19] R. Kumar, R. K. Shukla, A. Kumar, and A. Kumar, "A computational study on air entrapment and its effect on convective heat transfer during droplet impact on a substrate," *Int. J. Therm. Sci.*, vol. 153, p. 106363, Jul. 2020, doi: 10.1016/J.IJTHERMALSCI.2020.106363.

[20] C. Guo, L. Liu, R. Yang, J. Lu, and S. Liu, "Bouncing Regimes of Supercooled Water Droplets Impacting Superhydrophobic Surfaces with Controlled Temperature and Humidity," *Langmuir*, vol. 39, no. 29, pp. 10199–10208, Jul. 2023, doi: 10.1021/ACS.LANGMUIR.3C01099/ASSET/IMAGES/MEDIUM/LA3C01099_0012.GIF.

[21] Y. Xu, L. Tian, C. Zhu, and N. Zhao, "Reduction in the contact time of droplet impact on superhydrophobic surface with protrusions," *Phys. Fluids*, vol. 33, no. 7, 2021, doi: 10.1063/5.0055565.

[22] N. N. Han, S. W. Wang, B. M. Sun, and X. He, "Nanodroplet impacts on hydrophobic/superhydrophobic surfaces with point textures," *J. Appl. Phys.*, vol. 132, no. 20, Nov. 2022, doi: 10.1063/5.0109464/2837925.

[23] A. Gauthier, S. Symon, C. Clanet, and D. Quéré, "Water impacting on superhydrophobic macrotextures," *Nat. Commun.*, vol. 6, pp. 2–7, 2015, doi: 10.1038/ncomms9001.

[DOI: 10.22068/ase.2024.685]

[24] E. Vazirinasab, K. Maghsoudi, R. Jafari, and G. Momen, "A comparative study of the icephobic and self-cleaning properties of Teflon materials having different surface morphologies," *J. Mater. Process. Technol.*, vol. 276, p. 116415, 2020, doi: 10.1016/j.jmatprotec.2019.116415.

[25] R. Attarzadeh and A. Dolatabadi, "Icephobic performance of superhydrophobic coatings: A numerical analysis," *Int. J. Heat Mass Transf.*, vol. 136, pp. 1327–1337, 2019, doi: 10.1016/j.ijheatmasstransfer.2019.03.079.

[26] V. Kulkarni and P. E. Sojka, "Bag breakup of low viscosity drops in the presence of a continuous air jet," *Phys. Fluids*, vol. 26, no. 7, Jul. 2014, doi: 10.1063/1.4887817/258562.

[27] A. Balabel, "Numerical prediction of droplet dynamics in turbulent flow, using the level set method," *Int. J. Comut. Fluid Dyn.*, vol. 25, no. 5, pp. 239–253, Jun. 2011, doi: 10.1080/10618562.2011.594795.

[28] A. Chahine, J. Sebilleau, R. Mathis, and D. Legendre, "Caterpillar like motion of droplet in a shear flow," *Phys. Rev. Fluids*, vol. 8, no. 9, p. 093601, Sep. 2023, doi: 10.1103/PHYSREVFLUIDS.8.093601/FIGURES/12/MEDIUM.

[29] F. Yeganehdoust, A. Amer, N. Sharifi, I. Karimfazli, and A. Dolatabadi, "Droplet Mobility on Slippery Lubricant Impregnated and Superhydrophobic Surfaces under the Effect of Air Shear Flow," *Langmuir*, vol. 37, no. 20, pp. 6278–6291, May 2021, doi: 10.1021/ACS.LANGMUIR.1C00726/SUPPL_FILE/LA1C00726_SI_001.PDF.

[30] S. Moghtadernejad, M. Tembely, M. Jadidi, N. Esmail, and A. Dolatabadi, "Shear driven droplet shedding and coalescence on a superhydrophobic surface," *Phys. Fluids*, vol. 27, no. 3, Mar. 2015, doi: 10.1063/1.4914168/259697.

[31] C. W. Hirt and B. D. Nichols, "Volume of fluid (VOF) method for the dynamics of free boundaries," *J. Comput. Phys.*, vol. 39, no. 1, pp. 201–225, Jan. 1981, doi: 10.1016/0021-9991(81)90145-5.

[32] J. U. Brackbill, D. B. Kothe, and C. Zemach, "A continuum method for modeling surface tension," *J. Comput. Phys.*, vol. 100, no. 2, pp. 335–354, Jun. 1992, doi: 10.1016/0021-9991(92)90240-Y.

[33] Š. Šikalo, H.-D. Wilhelm, I. V Roisman, S. Jakirlić, and C. Tropea, "Dynamic contact angle of spreading droplets: Experiments and simulations," *Phys. Fluids*, vol. 17, no. 6, p. 62103, May 2005, doi: 10.1063/1.1928828.

[34] F. M. White, *Fluid mechanics*, 7th ed. McGraw-Hill, 2011.

[35] W. M. Haynes, *Handbook of chemistry and physics*, 95th ed. Boca Raton, Florida, 2014.

[36] D. Khojasteh, M. Kazerooni, S. Salarian, and R. Kamali, "Droplet impact on superhydrophobic surfaces: A review of recent developments," *J. Ind. Eng. Chem.*, vol. 42, pp. 1–14, Oct. 2016, doi: 10.1016/J.JIEC.2016.07.027.

[37] H. Wang *et al.*, "Bouncing behavior of a water droplet on a super-hydrophobic surface near freezing temperatures," *Int. J. Heat Mass Transf.*, vol. 174, p. 121304, Aug. 2021, doi: 10.1016/J.IJHEATMASSTRANSFER.2021.121304.

[38] X. Zhang, X. Liu, X. Wu, and J. Min, "Simulation and experiment on supercooled sessile water droplet freezing with special attention to supercooling and volume expansion effects," *Int. J. Heat Mass Transf.*, vol. 127, pp. 975–985, 2018, doi: 10.1016/j.ijheatmasstransfer.2018.07.021.

[39] K. Shi, J. Huang, and X. Duan, "An analytical framework for predicting the total freezing delay time of water droplet impact on hydrophobic solid surfaces," *Int. J. Therm. Sci.*, vol. 196, p. 108726, Feb. 2024, doi: 10.1016/J.IJTHERMALSCI.2023.108726.

[40] A. Criscione, I. V. Roisman, S. Jakirlić, and C. Tropea, "Towards modelling of initial and final stages of supercooled water solidification," *Int. J. Therm. Sci.*, vol. 92, pp. 150–161, 2015, doi: 10.1038/ncomms1630.

[41] Y. Wang, L. Ju, D. Han, and Q. Wang, "Numerical investigation of the impacting and freezing process of a single supercooled water

[DOI: 10.22068/ase.2024.685]

droplet," *Phys. Fluids*, vol. 33, no. 4, 2021, doi: 10.1063/5.0048206.

[42] J. Blake, D. Thompson, D. Raps, and T. Strobl, "Simulating the freezing of supercooled water droplets impacting a cooled substrate," *AIAA J.*, vol. 53, no. 7, pp. 1725–1739, 2015, doi: 10.2514/1.J053391.

[43] A. Inc., "ANSYS Fluent User Guide." ANSYS Inc, 2020.

[44] X. Zhang, X. Liu, X. Wu, and J. Min, "Impacting-freezing dynamics of a supercooled water droplet on a cold surface: Rebound and adhesion," *Int. J. Heat Mass Transf.*, vol. 158, p. 119997, 2020, doi: 10.1016/j.ijheatmasstransfer.2020.119997.

[45] A. Mohammad Karim, "A review of physics of moving contact line dynamics models and its applications in interfacial science," *J. Appl. Phys.*, vol. 132, no. 8, p. 80701, Aug. 2022, doi: 10.1063/5.0102028/2837259.

[46] S. F. Kistler, "Hydrodynamics of Wetting," in *Wettability*, John Berg, Ed., CRC Press, 1993.

[47] B. Ji, Q. Song, and Q. Yao, "Numerical study of hydrophobic micron particle's impaction on liquid surface," *Phys. Fluids*, vol. 29, no. 7, p. 77102, 2017.

[48] H. Chen, X. Liu, K. Wang, H. Liu, and S. Shen, "Numerical study on dynamic characteristics of double droplets impacting a super-hydrophobic tube with different impact velocities," *Int. J. Comut. Fluid Dyn.*, vol. 33, no. 5, pp. 222–233, May 2019, doi: 10.1080/10618562.2019.1666111.

[49] A. Balabel, "Numerical simulation of two-dimensional binary droplets collision outcomes using the level set method," *Int. J. Comut. Fluid Dyn.*, vol. 26, no. 1, pp. 1–21, Jan. 2012, doi: 10.1080/10618562.2011.639767.

[DOI: 10.22068/ase.2024.685]